



Molecular dynamics simulations of tensile response for FeNiCrCoCu high-entropy alloy with voids

Tinghong Gao^{*}, Han Song, Bei Wang, Yue Gao, Yutao Liu, Quan Xie, Qian Chen, Qingquan Xiao, Yongchao Liang

Institute of Advanced Optoelectronic Materials and Technology, College of Big Data and Information Engineering, Guizhou University, Guiyang 550025, China



ARTICLE INFO

Keywords:

Void defects
High entropy alloy
Tensile strength
Molecular dynamics simulation
Material deformation
Young's modulus

ABSTRACT

While preparing and using high entropy alloys (HEAs), many defects such as voids are inevitably formed. The effects of voids on the mechanical properties of FeNiCrCoCu HEAs are investigated using molecular dynamics simulations. The evolution of voids is examined by using models with one or two voids considering different void sizes, applied strain rates, and temperatures. The results demonstrate that the existence of the voids does influence the mechanical properties of HEAs. The tensile strength of the single-void model is higher than that of double-void model. The stress-strain curves demonstrate that a larger initial void size could reduce the tensile strength. During the tensile deformation, all dislocation emission occurs initially from the surface of the void. However, it occurs between the two voids in double-void models, which causes the deformation of the voids. With temperature increases, the tensile strength decreases. Under various strain rates, the tensile strength slightly rises at strain rates ranging from 10^8 to 10^9 s^{-1} . However, it significantly increases at a strain rate of 10^9 to 10^{10} s^{-1} .

1. Introduction

High-entropy alloys (HEAs) with a high mixing entropy are solid solutions having five or more elements [1–4], which have a simple crystal structure, such as face-centered cubic (FCC), body-centered cubic (BCC), or hexagonal close-packed (HCP) arrangements [5–8]. HEAs have excellent mechanical properties [9–12], including high hardness and strength [13–15], good corrosion resistance [16–18], high wear resistance [19,20], high-temperature stability [21,22], and high-strain-rate superplasticity [23–25]. A newly developed Ni₃₅(C-₀Fe)₅₅V₅Nb₅ HEA [26] has high yield strength (855 MPa), high ultimate tensile strength (1302 MPa), and incredible elongation (50%). The HCP transformation at 223 K can make the Fe₄₀Mn₄₀Co₁₀Cr₁₀ HEAs harder than 298 K, where deformation twinning occurs [27]. The increase in percentage of Al and Ti increases the tensile strength of the CoCrFeNi (Al_{0.3}Ti_{0.2})_x HEA [28]. The research on the mechanical properties of nonequiautomic FeCrNiCoMn HEAs [29] shows that the adjustment of element proportion can change the tensile strength. Therefore, a further study in HEAs is very important for many promising applications in engineering fields.

Among many HEAs, FeNiCrCoCu HEAs with a simple FCC solid-

solution structure [30–33] have attracted considerable attention recently in many studies [34–37]. For nanoindentation tests, the high dislocation density made the material strongly harden, and plentiful slip systems stimulated made the good plasticity of FeNiCrCoCu HEAs [38], which is the origin of the high strength and toughness process revealed by molecular dynamics (MD) simulations. For the FeNiCrCoCu HEAs having twin boundaries, the twinning layer could confine dislocation slip and nucleation, thus affecting plastic deformation [39] during nanoindentation. The movement of grain boundary and dislocations is important for softening [40] in nanocrystalline FeNiCrCoCu HEAs during the tensile process where the inverse Hall-Petch relationship was reported for the first time via the MD simulation. Coating FeNiCrCoCu HEA on a Cu substrate demonstrated that the FeNiCrCoCu HEAs have good protective properties, effectively protecting the Cu substrate from wear during a cutting process [41]. The high radiation resistance in FeNiCrCoCu HEA compared with a pure Ni model and average atom model may be attributed to the long-term evolution of defects [42]. During the rapid solidification, different nucleation modes of nondirectional and directional growths in FeNiCrCoCu HEAs were observed. Moreover, a nested tetrahedral lamellar structure formed in directional growth nucleation mode [43]. Because of the excellent strength and

* Corresponding author.

E-mail address: gaotonghong@sina.com (T. Gao).

plasticity of FeNiCrCoCu HEA, it is the subject of study in this work.

Commonly, while preparing and using alloys, a considerable number of defects are inevitably formed. Selective laser melting (SLM), one of the additive manufacturing (AM) techniques, typically uses high-powered laser energy for SLM metal alloys and metal matrix composite materials layer upon layer. Material characteristics can lead to porosity defects [44–46]. In the selective laser melting process with pure *in-situ* Ag as a powder, the generation and distribution of pore defects are influenced by the difference in laser scan speed and hatch distances. The sample density increases by reducing the scanning speed and hatch distance [47]. While fabricating binary copper-silver (CuAg) alloy by *in situ* alloying, pore defect morphology and distribution can be controlled by the Ag content. The results demonstrated that increased Ag content could effectively reduce the number of pores and the average pore diameter of CuAg [48]. Usually, void defects are formed in materials and have an important influence on their mechanical properties because voids' nucleation, growth, and coalescence are related to the material failure [49–51]. In single crystal copper, the growth and coalescence of two voids is the primary failure mechanism of ductile metals [52]. It is shown that twin boundary and void defects affect the mechanical property during the uniaxial tensile deformation of bulk nanotwinned Cu. The yield stress decreases with increased void size [53]. The mechanical properties of Ni-based superalloys with void defects and different phase structures decreased by dislocation reaction and aggregation [54]. In CoCrFeMnNi HEAs, the addition of spherical voids or HCP phase inclusions demonstrated different effects on the mechanical property, and the parallel twins and dislocation junctions caused by void defects significantly improved the strength of HEAs [55]. At a low temperature of 1 K, voids growth in CoCrFeMnNi HEAs was suppressed compared with Ni metal or Ni-based binary alloys [56]. Although these studies demonstrated the presence of voids effects on the mechanical properties in traditional metals or other HEAs, the impact mechanism of voids on FeNiCrCoCu HEAs remains elusive; therefore, it is important to examine the impact mechanism of voids on the mechanical properties of FeNiCrCoCu HEAs.

In this study, we primarily investigated the effects of the void size, strain rate, and temperature on the deformation behavior of FCC-FeNiCrCoCu HEA with voids. We elucidate the effect of voids on the deformation mechanism during tensile loading. Section 2 and Section 3 describe the computational methods and results. The future challenge and conclusions are discussed in Sections 4 and 5.

2. Simulation method and conditions

Equiatomic single-crystal FCC-FeNiCrCoCu HEA was used to study uniaxial plastic deformation. The initial model with an FCC lattice spacing of 3.62 Å [57] has a size of 50 Å × 257 Å × 257 Å (length ×

width × height, respectively), containing between 265,406 and 288,942 atoms. The crystallographic orientations of the model are: x: [100], y: [010], z: [001]. In this study, cylindrical voids were added to examine the influence of voids on the mechanical property of models. The void defects had a radius of 10, 15, 20, 25, or 30 Å; the effects of single or double void in the model were examined. For double-void models [58–60], the spacing between two voids is set to the diameter of the void. Fig. 1 shows the single and double-void models with a void radius of 20 Å.

The embedded atom model potential [61] was used to simulate the tensile deformation of FCC single-crystal FeNiCrCoCu HEA with void defects in all simulations where the NPT ensemble [62] was applied with a fixed time step of 1 fs. Periodic boundary conditions were adopted along the X- and Y- directions. However, the Z- direction had a free boundary condition. Before tensile deformation, to obtain a state of minimum energy, the temperature and pressure control are achieved using the Nosé-Hoover thermostat and barostat [63], respectively. However, the integration of the motion equation is realized using the velocity-Verlet algorithm [64]. Then, the model was relaxed for 50 ps at a specific temperature to achieve a thermodynamic equilibrium state, and the pressure in the X- and Z-directions was maintained at 0 bar. During the tensile deformation, strain rates of 1×10^8 , 5×10^8 , 1×10^9 , 5×10^9 , or 1×10^{10} s⁻¹ were applied along the Y-direction. Moreover, different temperature conditions were evaluated (300, 600, or 900 K).

All simulations were performed using the open-source large-scale atomic/molecular massively parallel simulator (LAMMPS) [65–67]. The structural analysis and visualization were performed using OVITO [68], with the dislocation extraction algorithm [69] and common neighbor analysis (CNA) [70].

3. Results and discussion

3.1. Void size effects

This section examines the effect of void size on the plastic deformation behavior of FeNiCrCoCu HEA models with void defects during the uniaxial tension. The change of tensile strength, Young's modulus, flow stress, peak stress, phase transformation, and shear strain distribution by the void defect was uncovered. Moreover, we compare the mechanical properties of models with void defects and the model without voids.

3.1.1. Single-void model

The uniaxial stress-strain responses of different single-void models along the Y-direction under a strain rate of 1×10^9 s⁻¹ at 300 K are shown in Fig. 2(a). The results of the model without void are shown for comparison. All curves linearly increase to the peak stress value at the

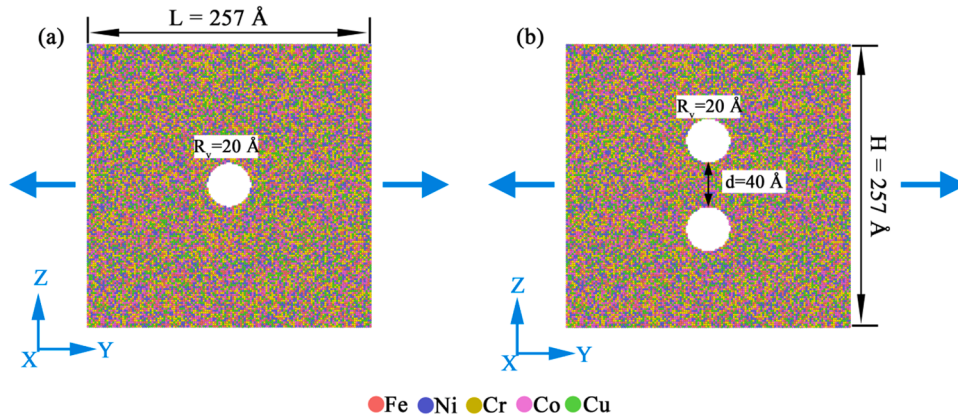


Fig. 1. Simulation model of FeNiCrCoCu HEA, which has a void with the size of $R_v = 20$ Å (R_v is the radius of the void defect): (a) single-void model; (b) double-void model (the distance between two voids is 40 Å).

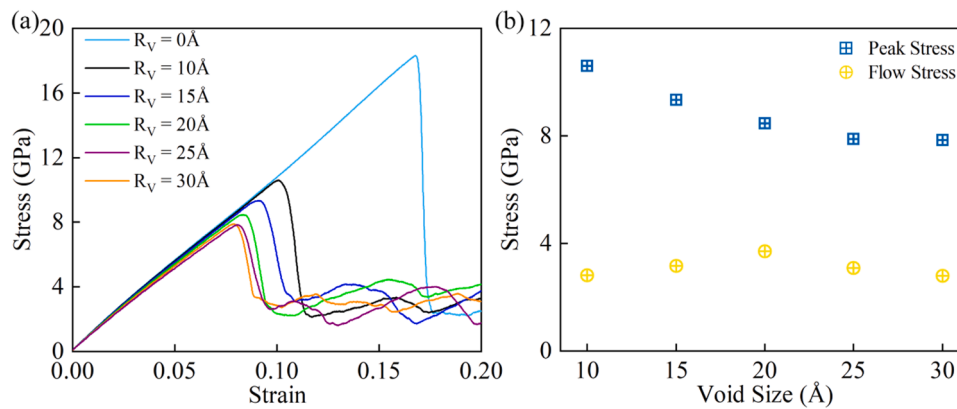


Fig. 2. (a) Tensile stress–strain curves of single-void FeNiCrCoCu HEAs with different void sizes of $R_V = 0\text{--}30\text{ \AA}$ at a strain rate of $1 \times 10^9\text{ s}^{-1}$ at 300 K (R_V is the radius of the void defect); (b) Influence of void size on the peak stress and flow stress for single-void FeNiCrCoCu HEA.

elastic deformation stage. The tensile strength determined from the no-void model (18.3 GPa) is much higher than that of the single-void model with a void size of 10 \AA (10.6 GPa), which suggests the presence of the void degrades the stretching properties of the FeNiCrCoCu HEAs. This is consistent with previous researches [36,71,72]. Moreover, it is evident that the peak stress is negatively correlated with the void size, and the model with a smaller void could bear greater peak stress in Fig. 2(b). When the void size increases, the strain value corresponding to the peak stress reduces. The agreement result has been also detected in the previous study by Qi et al. [55] under the tensile process with void-FeNiCrCoMn HEAs using MD simulation. In experiments, similar results have been reported for Ag microwires [73] and ladies' finger natural fiber specimens [74], respectively. At the plastic deformation stage, the stress sharply drops with the increase in strain, and then the curve fluctuates. To better understand the change of stress at this stage, the flow stress is calculated as the average of the stresses over the strain range of 0.11–0.2. The flow stress is 2.82, 3.15, 3.7, 3.08, and 2.79 GPa, corresponding to the model with the void size of 10, 15, 20, 25, and 30 \AA , respectively. In this study, the void sizes have little effect on the flow stress.

To evaluate the effect of voids on structure and phase transformation, Fig. 3 shows the dynamic responses of single-void FeNiCr-CoCu HEAs with different void sizes under different strain values at 300 K. Dislocation emission initially occurs from the surface of the void on both sides perpendicular to the Z- direction before the peak stress point is reached compared with the stress–strain curves above. The appearance of dislocation and phase transformation tends to be earlier as the void size increases. The strain values at the start of dislocation emission and phase transformation are 0.106, 0.89, 0.81, 0.79, and 0.78, corresponding to the models with void sizes of 10, 15, 20, 25, and 30 \AA . A short time after the stress reaches the peak value, additional dislocations are formed because of stacking faults and twin structures in the materials, and many atoms change from the FCC structure to HCP structure. Thinner twinning in fcc-based high entropy alloys can enhance strength to some extent [75,76]. As the strain increases, the interaction among dislocations results in the formation and disappearance of dislocations, resulting in fewer dislocations than those observed in Fig. 3 (a3–e3). As shown in Fig. 3(a4–e4), as the strain reaches to 0.2, the phase transformation is inversely proportional to the void size. A void size of 30 \AA results in the lowest percentage of HCP atoms.

The trend of the dislocation density of single-void FeNiCrCoCu HEA as a function of strain and void size is shown in Fig. 4(a). The dislocation density vigorously increases in all models till the yield point, after which the dislocation density shows a slightly fluctuating trend as strain values increase. Maximum dislocation densities decrease with increasing void size. After reaching the peak stress, the dislocation density demonstrates the same trend for all models: first reducing and then increasing. This

can be explained by the gradual increase in dislocation density caused by the strong increase in phase transformation from the FCC phase to another structure after the peak stress point, which results in the slow increase of dislocation density. At the strain value of 0.2, the HEA with a void size of 10 \AA has the highest total dislocation density, whereas that of the HEA with a void size of 15 \AA is the lowest, indicating that the dislocation density has no clear relationship with void size at the end of tensile deformation. Young's modulus is identified as the slope of the stress–strain curve before the dislocation nucleation [77]. Fig. 4(b) shows the relationship between Young's modulus and void size. Adding voids clearly reduces Young's modulus. The model with a void size of 10 \AA affords the highest Young's modulus and has a high tensile strength.

3.1.2. Double-void model

Fig. 5(a) shows the uniaxial stress–strain curves of double-void HEA models with different void sizes calculated using MD simulations. Similar to the case of single-void HEAs, the tensile strength is reduced with the increase in void size. In Fig. 5(b), the peak stresses are lower than those of the single-void HEAs and inversely dependent on void size. Therefore, the increase in the number and void size degrades the tensile strength of materials. The flow stress is insensitive to the increasing void size. Fig. 5(c) shows the dislocation density of double-void HEA models with different void size. At the elastic stage, the dislocation density sharply increases for all models. Each model demonstrates a different variation tendency at the plastic stage. For models with a void size of 10 or 25 \AA , the dislocation density decreases and then increases after the peak stress point. However, the dislocation density of models with a void size of 15 or 20 \AA declines with certain fluctuations. For the model with the largest void size, the dislocation density greatly decreases, which is different from the behavior of other models. The dislocation density in each model is independent of the void size at the end of the tensile process, and the model with 15 \AA has the highest dislocation density. Fig. 5(d) shows that Young's modulus from double-void HEA models decrease with the increase in void size.

To explore the influence of voids on tensile deformation, Fig. 6 shows the shear strain distribution within the double-void models at different strain values. Each atom is painted by the local shear strain value. Fig. 6 (a1–e1) shows the shear strain distribution corresponding to the peak stress for each void size where the local strain begins around the voids. However, in the models with smaller void sizes, a complete shear strain band is formed between the two voids, unlike that in models with larger void sizes. Furthermore, with the increasing void size, the initial strain value decreases. The shear strain sharply increases and propagates from the voids to the free surface (Fig. 6(a2–e2)). For a larger void size of 30 \AA , the strain is mainly concentrated around the void and does not propagate around the model (Fig. 6(e2)). The positional relationship of the two voids changes with an additional increase in the strain. The

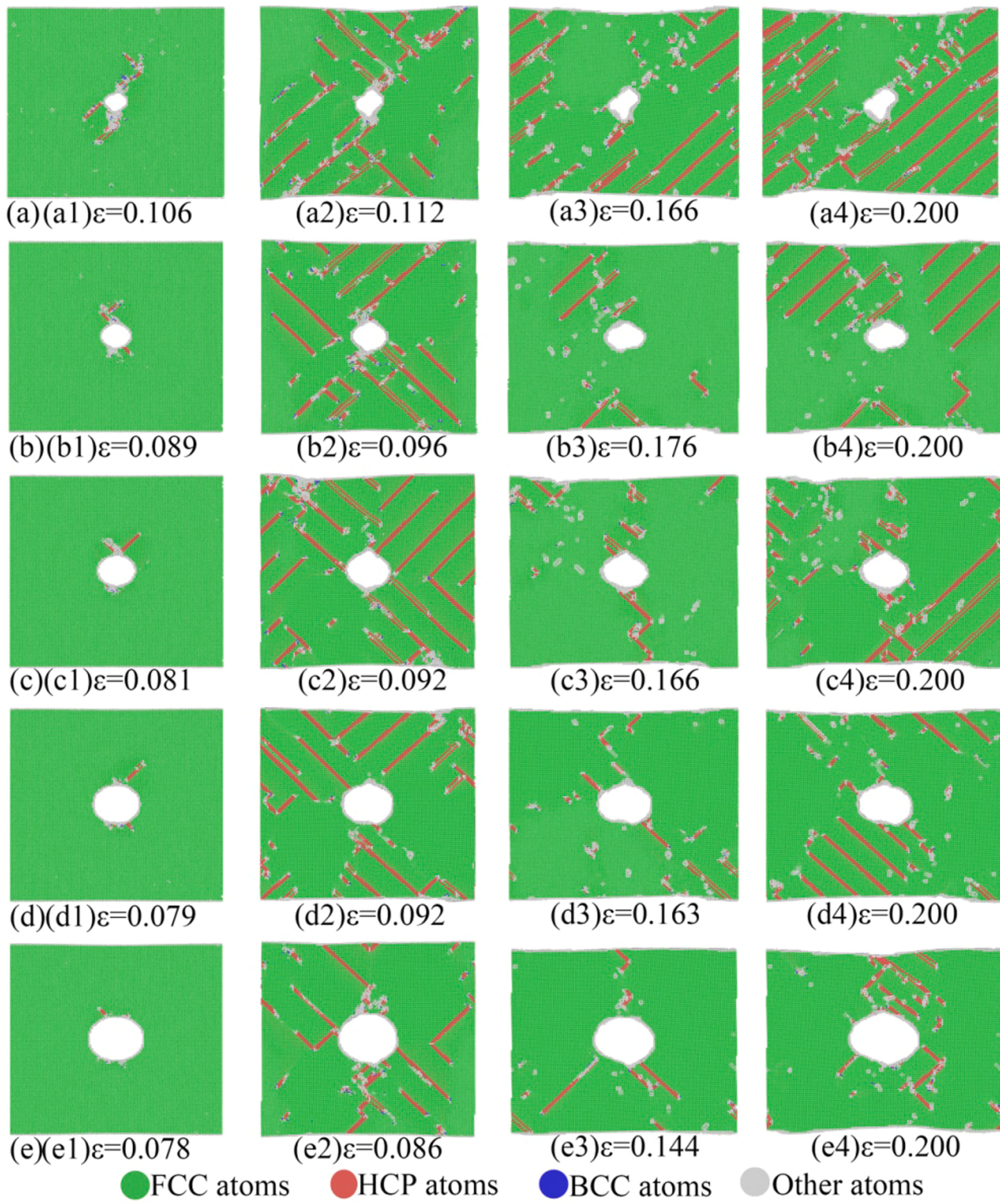


Fig. 3. Dynamic response of single-void FeNiCrCoCu HEA with different void sizes and strains at 300 K. (a) $R_V = 10 \text{ \AA}$, (b) $R_V = 15 \text{ \AA}$, (c) $R_V = 20 \text{ \AA}$, (d) $R_V = 25 \text{ \AA}$, (e) $R_V = 30 \text{ \AA}$. The green, blue, red, and white colors in (a)–(e) indicate atoms belonging to fcc, bcc, hcp, and undefined lattices, respectively.

larger local shear strain of the shear band forms between two voids whose shrinkage deformation results in the coalescence. This is not shown for the models with void sizes of 25 and 30 Å in Fig. 6(a3–e3). Finally, at the strain value of 0.2, the voids of each model shrink to varying degrees. Because of the coalescence of two voids, the deformation degree of these voids is higher in the models with void sizes of

10, 15, and 20 Å. The shape of voids retains the original appearance in the models with a void size of 25 and 30 Å in Fig. 6(a4–e4), indicating that the void size may be related to the void coalescence. The coalescence of voids leads to the sudden decrease of the stress-strain curve. The inter-void interactions can be understood as the shear stress and dislocation reaction between the shear slip bands. Under the same strain

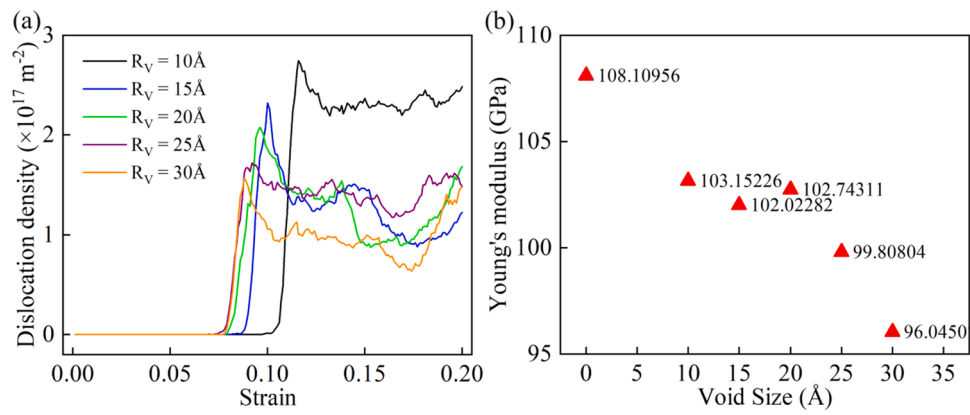


Fig. 4. (a) Dislocation density vs. strain; and (b) the influence of void size on the Young's modulus for single-void FeNiCrCoCu HEA.

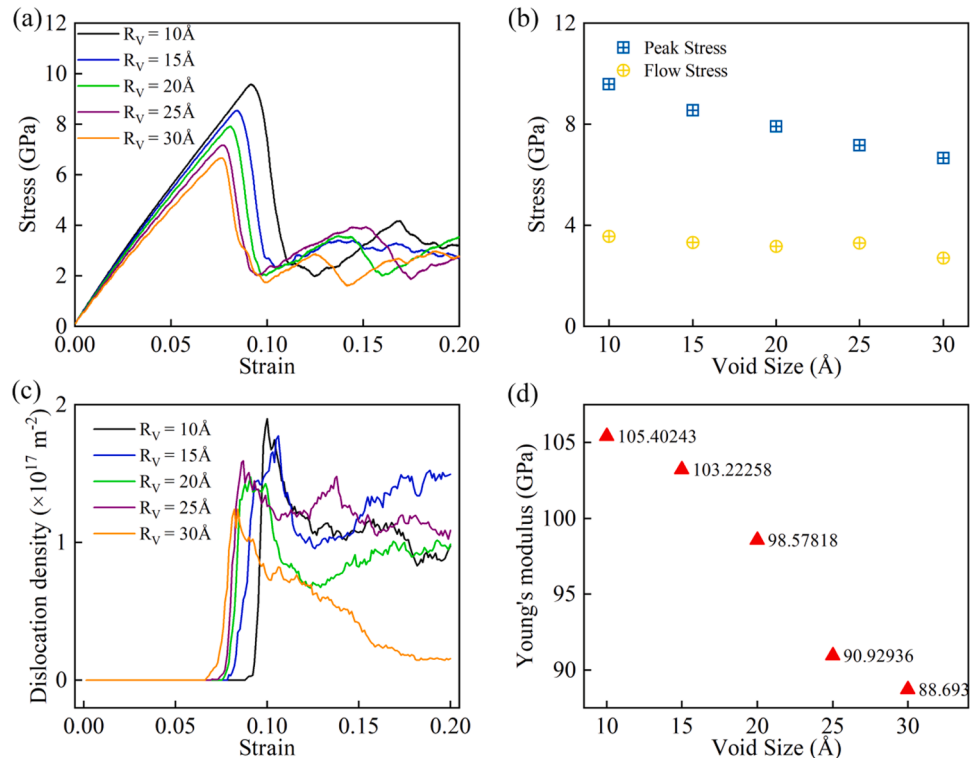


Fig. 5. Characterization results for double-void FeNiCrCoCu HEA with different void sizes. (a) Stress–strain curves were analyzed at a strain rate of $1 \times 10^9 \text{ s}^{-1}$ at 300 K; (b) The influence of void size on the peak stress and flow stress; (c) dislocation density vs. strain; and (d) The influence of void size on Young's modulus.

rate, models with larger void sizes would have adequate time and space to adapt to the tensile deformation, preventing the voids' deformation and coalescence. In addition, we also calculated the tensile results along the Z- loading direction at the same temperature and strain rate. Due to the little deformation of the voids, the peak stress and the flow stress is higher compared with Y- direction, as shown in the Fig. S1 and Table S1 in Supplementary Material. The dislocation emission still occurs from the surface of the voids, indicating that the voids are the main cause of the deformation in Fig. S2. The strain is concentrated on the surface of the voids and then spreads to the whole model to form a complete shear band. But compared with the Y- direction, the value of the shear strain is lower.

The dynamic responses of double-void FeNiCrCoCu HEAs are analyzed through CNA analysis to understand the changes of these two voids under tension, and the change tendency is shown in Fig. 7. At the beginning of the tensile process, dislocations primarily nucleate between

the two voids and the atoms of FCC phase convert to amorphous or HCP phase. With the increase in strain, the amorphous phase is dominant between the two voids and forms an amorphous band perpendicular to the tensile direction, which results in the two voids connected (Fig. 7 (a–c)). In models having larger void sizes, dislocation emission occurs from the voids on both sides perpendicular to the Z-direction. As the tensile deformation proceeds, dislocations and stacking faults are formed, and the atoms transform from the FCC phase to the amorphous phase between the voids. The dislocations and stacking faults inhibit the coalescence of voids.

3.2. Strain rate effects

In the abovementioned analysis, all the tensile simulations are performed at a strain rate of $1 \times 10^9 \text{ s}^{-1}$. To examine the strain rate effects on the material properties, the tensile deformation simulations are

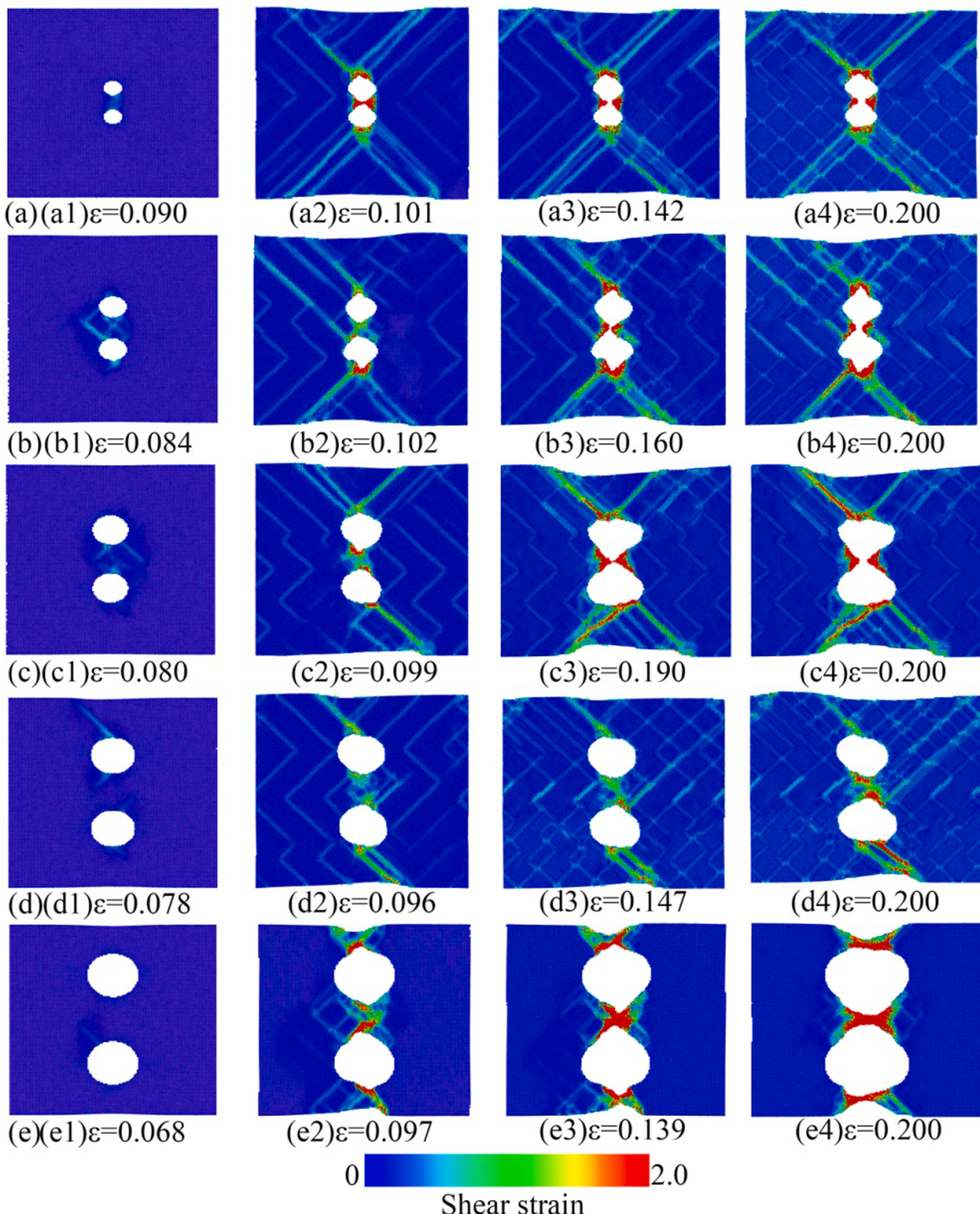


Fig. 6. Shear strain maps from double-void FeNiCrCoCu HEA models with different void sizes at different strain values at 300 K. Void sizes of (a) 10 Å, (b) 15 Å, (c) 20 Å, (d) 25 Å, or (e) 30 Å. The atoms are painted based on their von Mises strain value. All models have a strong shear strain concentration near the voids. Void coalescence happened in (a4–c4), whereas large deformation of the void happened in (d4–e4).

performed at different strain rates of 1×10^8 , 5×10^8 , 1×10^9 , 5×10^9 , and $1 \times 10^{10} \text{ s}^{-1}$. Fig. 8(a) and (c) demonstrates the stress-strain curves obtained from the single-void and double-void models with a void size of 25 Å at various strain rates. Based on the trends of stress-strain curves,

the tensile strength increases as the strain rate increases in both single-void and double-void models. At the elastic deformation stage, the strain value corresponding to the peak stress point is higher with increasing strain rates. Because the original stress in the model under higher strain

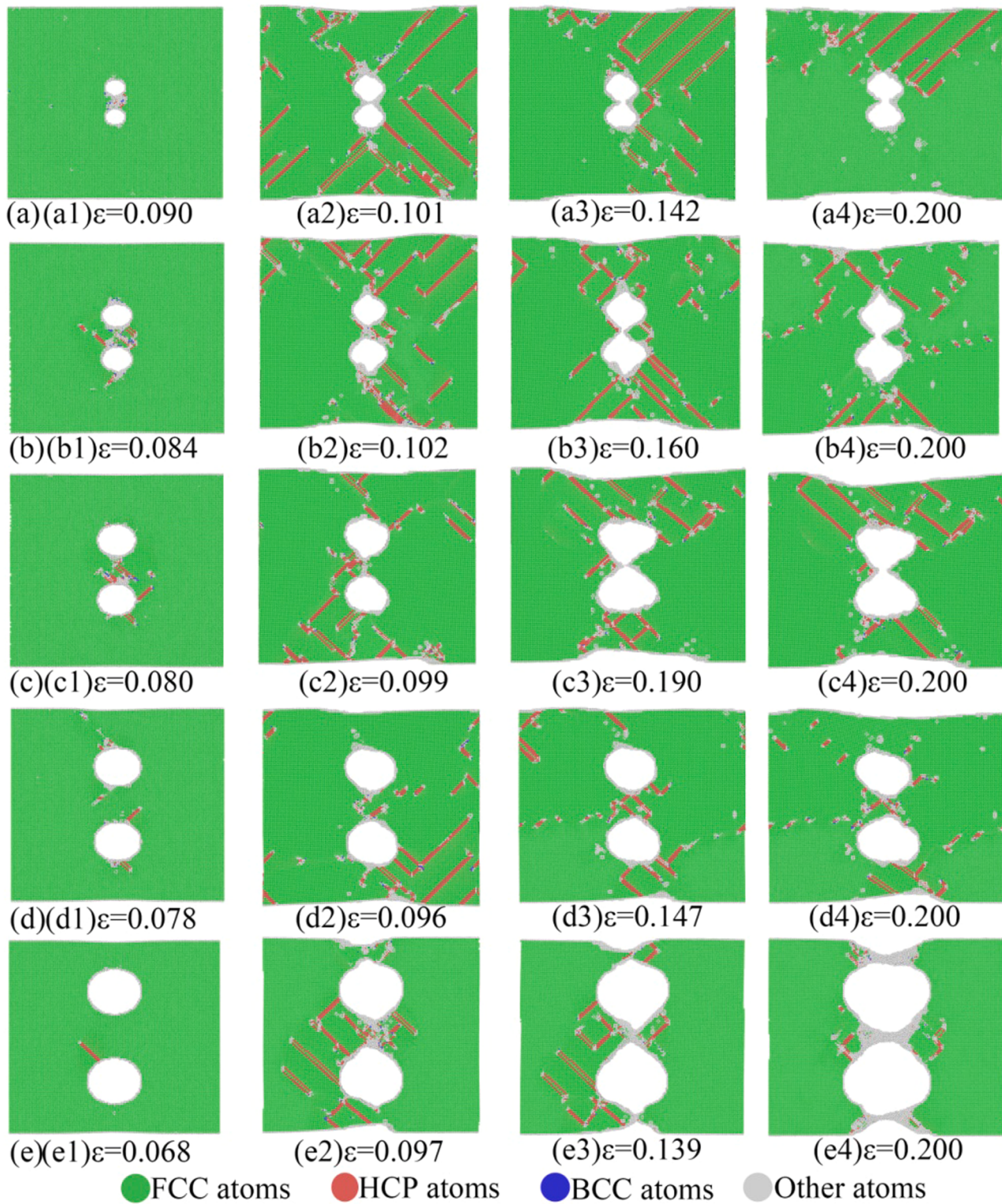


Fig. 7. Dynamic response of double-void FeNiCrCoCu HEA models at 300 K, various strain values, and void sizes of (a) 10 Å, (b) 15 Å, (c) 20 Å, (d) 25 Å, or (e) 30 Å. The green, blue, red, and white colors in (a)–(e) indicate atoms belonging to fcc, bcc, hcp, and undefined lattices, respectively.

rates takes considerable time to redistribute and relax, the released energy can balance the external energy of deformation or degradation needed for deformation growth. At the highest strain rate, the peak stress value reached is later compared with the lower strain rate. The stress value suddenly declines after reaching the peak stress point under the lowest strain rate. This is because the system has not fully relaxed

during FeNiCrCoCu HEAs deformation at a lowest strain rate. The phenomenon occurring in a short time period is conducive to the elastic properties of materials at the lowest strain rates.

Fig. 8(b) and (d) show the tensile strength and Young's modulus of both single-void and double-void models which have a void size of 25 Å at different strain rates. The tensile strength tends to rise with increasing

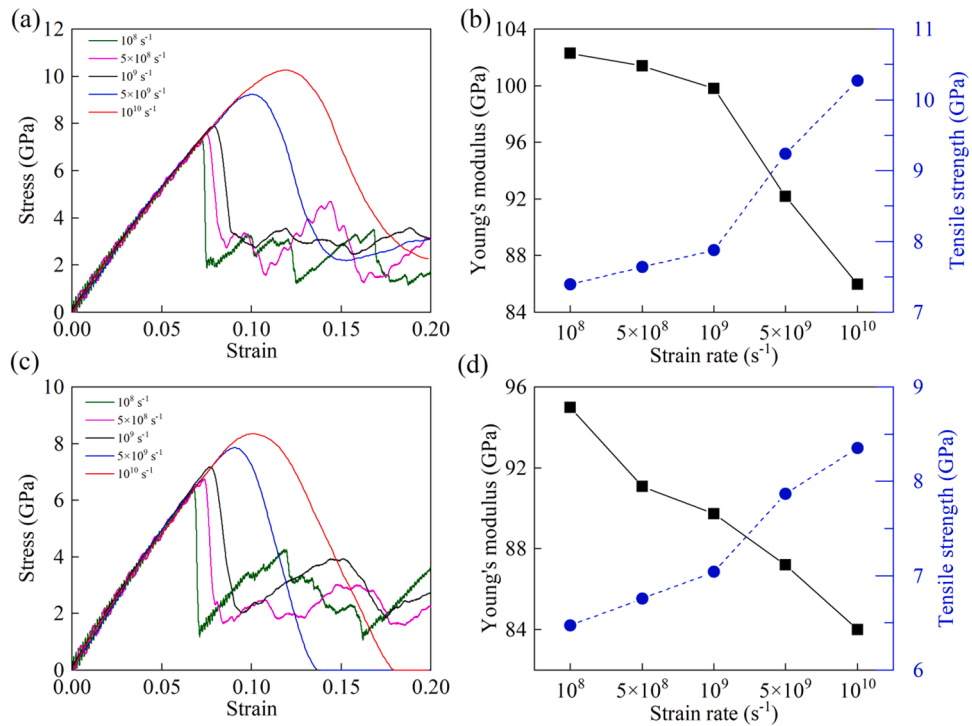


Fig. 8. Stress–strain curves from (a) single-void and (c) double-void HEA models with a void size of 25 Å under various strain rates; Young's modulus and tensile strength from (b) single-void and (d) double-void models with a void size of 25 Å at different strain rates.

strain rates, while the tensile strength more substantially increases from 1×10^9 to $5 \times 10^9 \text{ s}^{-1}$ than from 5×10^9 to $1 \times 10^{10} \text{ s}^{-1}$. By comparing single-void and double-void models, the tensile strength of the double-void model is lower than that of single-void model, indicating that the void defects degrade the material's mechanical properties. In both models, the same trend is observed with respect to Young's modulus. The Young's modulus decreases with the increasing strain rates. Young's modulus is related to load-bearing performance, which is reflected in strength characteristics. The increase in strain rate causes an increase in deformation density, increasing work hardening and yield stress. The more brittle the material, the greater the strain rate. The fracture is relatively easy to occur and vice versa. In previous studies, consistent results have been reported by Wang et al. [78] with CoNiFeAl_xCu_{1-x} HEAs, Doan et al. [79] with AlCrCuFeNi₂ HEAs, and Vu et al. [80] with Ni/Co multilayers during tensile deformation process using MD simulations.

3.2.1. Single-void model

Fig. 9 shows the dynamic response of single-void models under five strain rates by CNA analysis. It was evident that phase transformation, dislocations, and twins occurs in the system. Before reaching the peak stress point, dislocations nucleate on the top and bottom sides of the void. Higher strain rates result in the later nucleation time (Fig. 9 (a1–e1)). The dislocations rapidly expand around the void with increase in strain value. However, because the atoms are under considerable stress, large areas of the amorphous phase are formed under higher strain rates (Fig. 9(a3–e3)). At a strain value of 0.2, at the end of the tensile deformation process, the voids show different degrees of deformation. The degree of void deformation is larger with increase in strain rate. Furthermore, with increase in strain rates, the proportion of the amorphous phase significantly increases, indicating that the FCC phase is easier to convert to the amorphous phase under a higher strain rate (Fig. 9(a4–e4)). The results demonstrate that additional phase transformation occurs under higher strain rates.

3.2.2. Double-void model

Fig. 10 shows the distribution of shear strain of the double-void models at various strain values under different strain rates. The degree of void deformation increased with increase in strain rate. Fig. 10 (a1–e1) corresponds to the strain value at the peak stress point at different strain rates. The strain value at the beginning of deformation increases with increase in strain rates. As the tensile deformation process proceeds further, shear bands rapidly grow. As shown in Fig. 10 (a2–e2) and (a3–e3), the shear bands grow around the voids and quickly spread to the whole model under low strain rate conditions. However, the shear bands extend only in the Z-direction under higher strain rates. In Fig. 10 (a4–e4), the void is greatly deformed under higher strain rates because the material has no adequate time to relax and adapt to the high strain rate, thus leading to an excessive strain concentration around the voids (which does not occur under low strain rates). By stretching along the Z-loading direction under different strain rates, tensile strength increases with the increasing strain rates in Fig. S4. Strain is concentrated on the surface of the voids and spread to form an obvious shear band in all models, as shown in Figs. S3 and S5. The lower the strain rate, the more obvious the shear band.

The dynamic response from the double-void model under five strain rates as analyzed by CNA analysis was shown in Fig. 11. Fig. 11(a1–e1) shows the phase transformation of the double-void HEAs models at the peak stress where the strain of phase transformation is lower than that from the single-void model. The phase transformation can occur in advance by adding voids. At a strain rate of $1 \times 10^8 \text{ s}^{-1}$, the model has sufficient time to adapt to the tensile deformation, and there is little phase transformation. The same phenomenon is observed along the Z-loading direction in Fig. S4. Only a few vacancy defects occur at a strain value of 0.2 in Fig. 11(a4). At a strain rate of $1 \times 10^9 \text{ s}^{-1}$, the voids are slightly deformed, and dislocations and twins are formed between these two voids. As the strain increases, the proportion of the HCP phase first rises and then reduces. However, at strain rates of 5×10^9 and $1 \times 10^{10} \text{ s}^{-1}$, a much amorphous phase is formed between the voids, and dislocations and twins are emitted around the voids. Similarly, the proportion of the HCP phase firstly increases and then decreases with increase

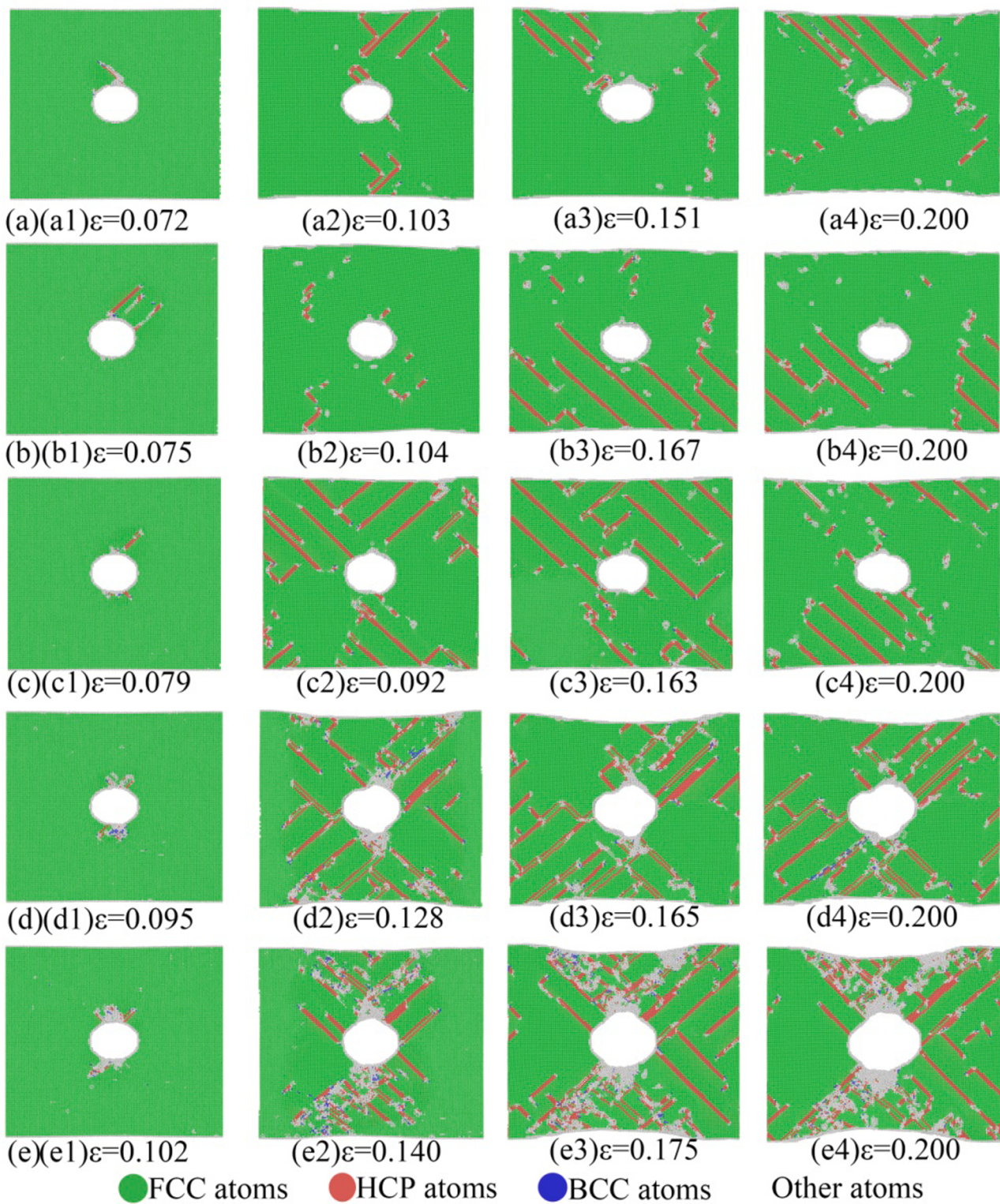


Fig. 9. Dynamic response from single-void FeNiCrCoCu HEA models, which have a void with the size of 25 Å at various strain values and 300 K at strain rates of (a) 1×10^8 , (b) 5×10^8 , (c) 1×10^9 s $^{-1}$, (d) 5×10^9 , or (e) 1×10^{10} s $^{-1}$. The green, blue, red, and white colors in (a)–(e) indicate atoms belonging to fcc, bcc, hcp, and undefined lattices, respectively.

in strain. The increase in strain rate can promote phase transformation to the amorphous phase.

3.3. Temperature effects

Temperature is one of the most important working conditions which affect the mechanical properties and deformation mechanism of materials. In the abovementioned analysis, all tensile simulations are

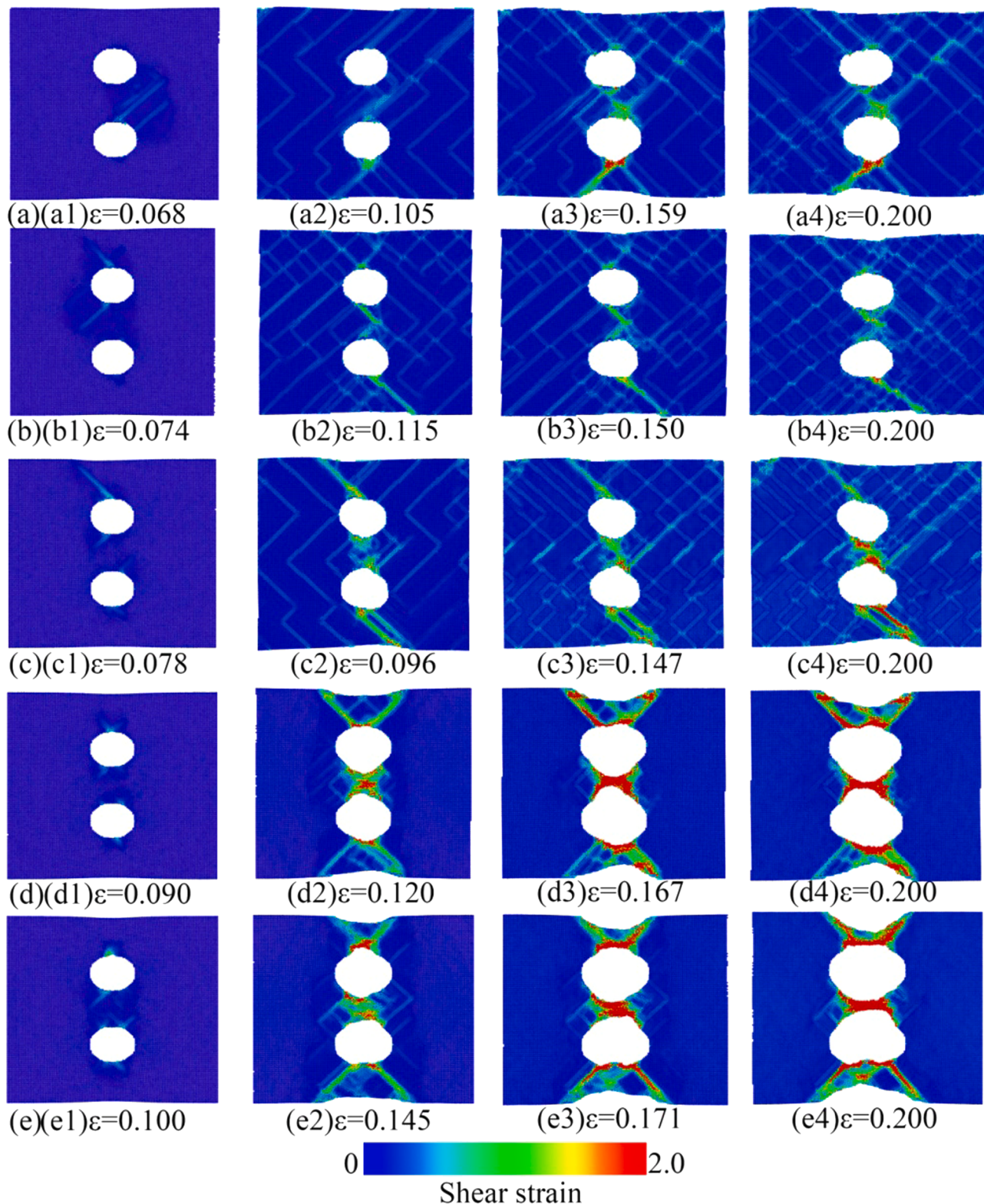


Fig. 10. Shear strains within double-void FeNiCrCoCu HEA that have a void with the size of 25 Å at various strain values and 300 K at strain rates of (a) 1×10^8 , (b) 5×10^8 , (c) 1×10^9 s $^{-1}$, (d) 5×10^9 , or (e) 1×10^{10} s $^{-1}$. The atoms are painted based on their von Mises strain value. Large shear strain is concentrated around the voids in all models. Many shear bands are produced at lower strain rates (a4–c4). The void is considerably deformed at a higher strain rate (d4–e4).

performed at 300 K. To examine the influence of temperature on the material properties, MD simulations of tensile deformation are performed at three constant temperatures of 300, 600, and 900 K. Fig. 12 shows the uniaxial stress-strain responses of both single-void and double-void models with a void size of 10 Å under the strain rate of $5 \times$

10^9 s $^{-1}$ at various temperatures. The tensile strength of the HEA decreases as the temperature increases. With the increase of temperature, the activation of atoms becomes stronger, and the fluctuation range of atoms near their equilibrium position becomes larger, which leads to the weakening of atomic bonds and the easier deformation of materials.

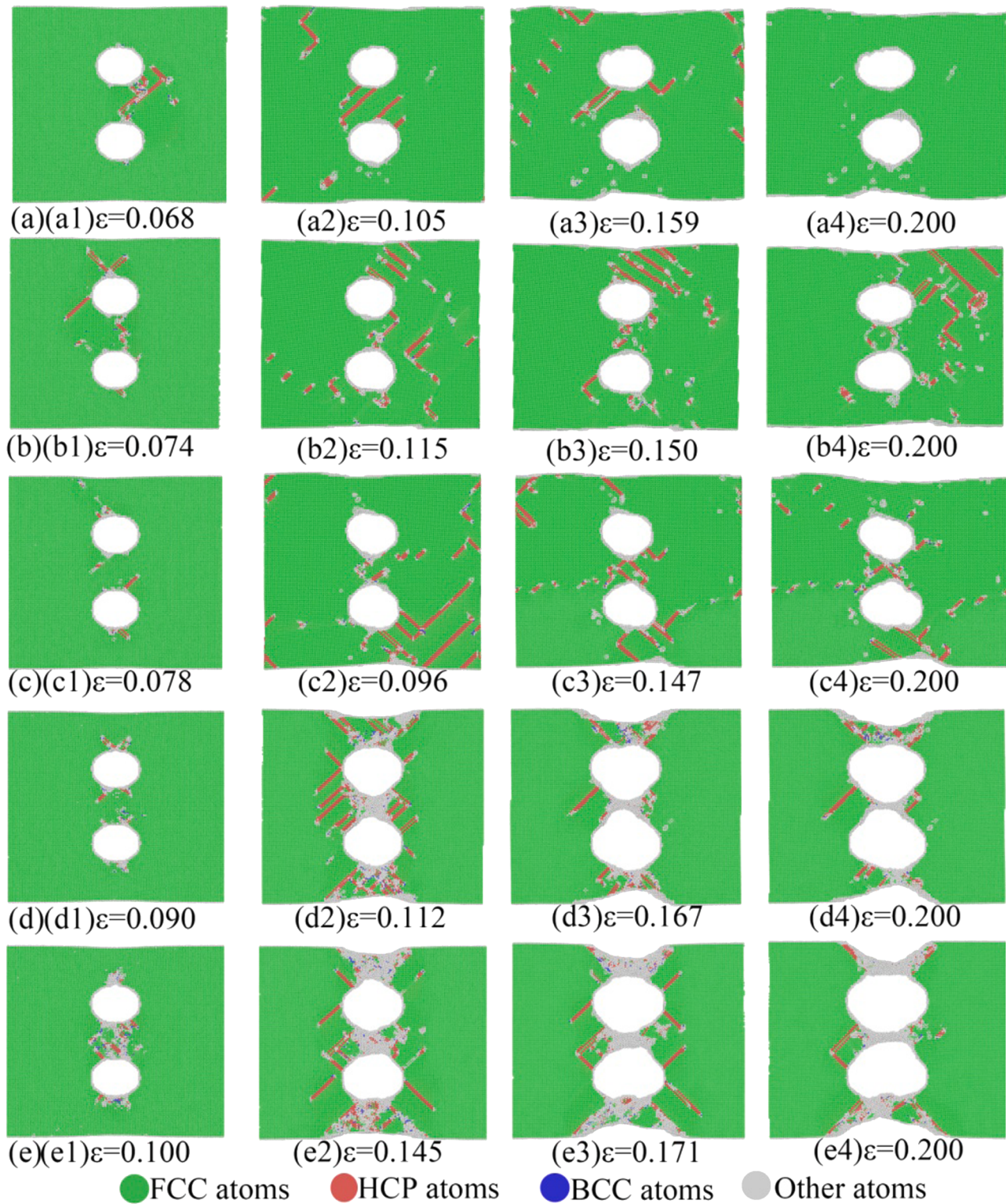


Fig. 11. Dynamic response of double-void FeNiCrCoCu HEAs, which have a void with the size of 25 Å at various strain values and 300 K under strain rates of (a) 1×10^8 , (b) 5×10^8 , (c) $1 \times 10^9 \text{ s}^{-1}$, (d) $5 \times 10^9 \text{ s}^{-1}$, or (e) $1 \times 10^{10} \text{ s}^{-1}$. The green, blue, red, and white colors in (a)–(e) indicate atoms belonging to fcc, bcc, hcp, and undefined lattices, respectively.

Therefore, the tensile strength is reduced. The brittleness of the material is higher at low temperature, while it is mainly soft at high temperature. Similar events have been observed in NiCo nanowires [81] and polycrystalline copper [82] in earlier research. In the initial low strain region, the slopes of the stress-strain curves at three temperatures are different. The slope of the curve is relatively small because the model

must release stress to adapt to the high temperature. Then, the curves increase to the peak stress with a constant slope, indicating that the slope of the curves is independent of temperature. After the stress reaches the tensile strength, it sharply reduces.

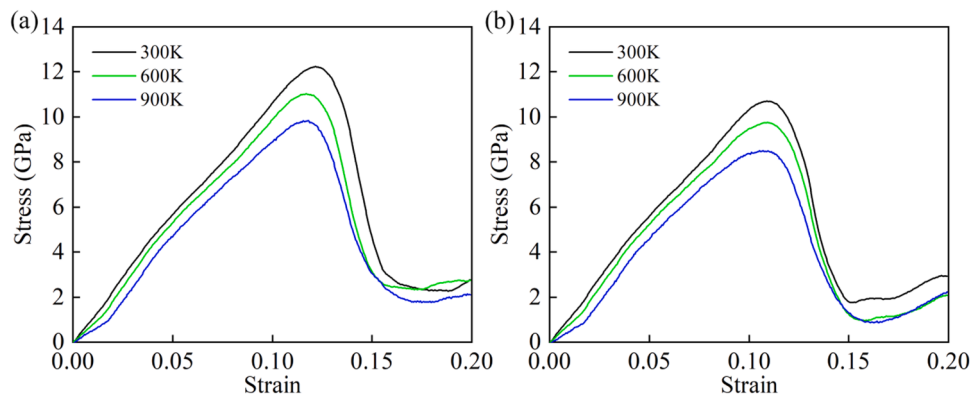


Fig. 12. Tensile stress-strain curves of FeNiCrCoCu HEAs with the void size of 10 Å at the strain rate of $5 \times 10^9 \text{ s}^{-1}$ at different temperatures: (a) single-void models; (b) double-void models.

3.4. Coupled effects of temperature and strain rate

To investigate the coupled effect of temperature and strain rate upon the mechanical properties, the tensile strength with the change of temperature and strain rate are presented in Fig. 13. The tensile strength of the double-void model is generally lower than that of the single-void models at the same temperature and strain rate. The tensile strength decreases with the increase in temperature and strain rate, showing that the tensile strength will decline under the simultaneous application of high temperature and high rate. Furthermore, the single-void HEA is more sensitive to the strain rate than the double-void one, particularly when the strain rate is reduced from 1×10^{10} to $5 \times 10^9 \text{ s}^{-1}$. Both single-void and double-void models demonstrate similarly sensitivity to the strain rate.

3.5. Distribution and evolution of dislocations

To understand the effect of voids on dislocation evolution, Fig. 14 shows the stress-strain curves and the distribution of different dislocations during the process of tensile deformation, where the illustrations are snapshots from the time of peak stress and the final state. The tensile strength of the single-void model is higher than that of the double-void model. At the stage of elastic deformation, the stress increased linearly with increased strain and there is no lattice distortion. When the stress at the edge of the void reaches the dislocation nucleation threshold, the dislocations initially nucleate on the surface of the voids. Dislocation nucleation on the surface of the void leads to stress relaxation, which is called as stress redistribution on the macro scale. Upon reaching the peak stress, all types of dislocations begin to nucleate from the single void and between the double voids. As the strain value increases, the

stress reduces. The sharp increase in dislocation length corresponds to the sudden decrease in stress. After peak stress, the material enters the yield stage and begins plastic deformation. The increase of void volume fraction and dislocation nucleation leads to the sudden decline of the system's ability to respond to the stress caused by a uniaxial stretch. Twin structures are formed at the end of tensile deformation in both models. Twin structures spread above the voids, and dislocations are concentrated in the double-void HEA. However, dislocations and twin structures are distributed over nearly the entire analyzed area in the single-void HEA.

During the uniaxial tensile deformation, the interaction between dislocations produces new dislocations, forming dislocation networks [83]. Shockley partial dislocations are the most common dislocations in metals with FCC structures. Stair-rod dislocations with a Burger vector of $1/6 <110>$ form due to the interaction of two Shockley partial dislocations whose motion is restricted in different planes. The stair-rod dislocations, stationary dislocation, cannot move on their slip plane, making work hardening of materials. Stair-rod dislocations are well known as barriers to dislocation motion. The presence of a larger number of stair-rod dislocations accumulated in FeNiCrCoCu HEAs helps to suppress shear band penetration. Furthermore, the formation of perfect dislocations with a Burger vector of $1/2 <110>$ also originates from Shockley dislocation. The interaction between the subsequent and conductive parts results in another fixed dislocation known as the Hirth dislocation, whose Burgers vector is $1/3 <100>$. A part of the {111} plane is also inserted or extracted, forming Frank dislocations with a Burger vector $1/3 <111>$.

The situation of the double-void model is similar to that of the single-void, which will be taken as an example in the dislocation analysis below. Fig. 15 shows the distribution of dislocations of the single-void

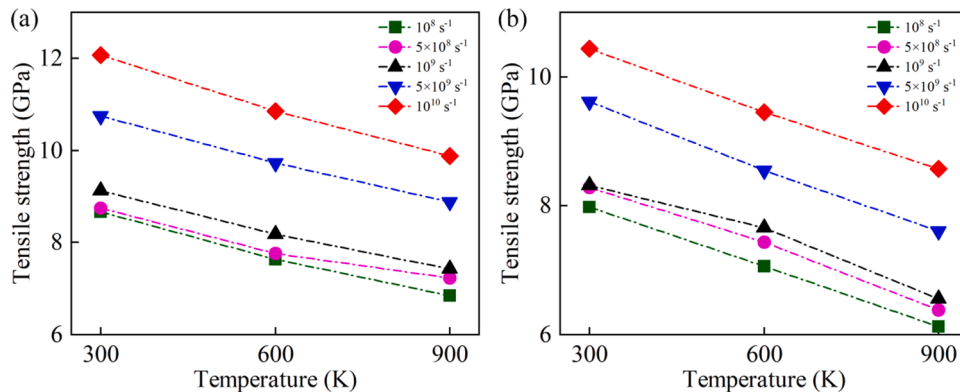


Fig. 13. Temperature dependence of the tensile strength in FeNiCrCoCu HEA with a void size of 15 Å under different strain rates. (a) single-void model; (b) double-void model.

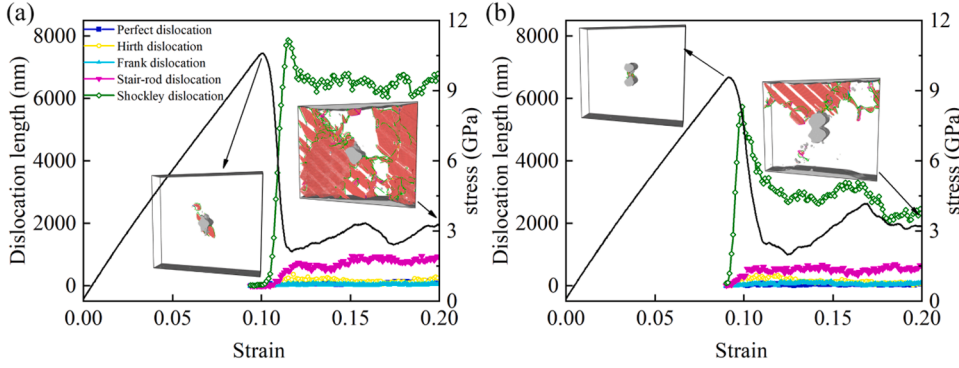


Fig. 14. Stress-strain curve and the distribution of different dislocations from the (a) single-void and (b) double-void models of FeNiCrCoCu HEA with the void size of 10 Å at a strain rate of $1 \times 10^9 \text{ s}^{-1}$ and 300 K. Dislocations are colored according to their dislocation styles. Red: other; Green: $1/6<112>$; Blue: $1/2<1 10>$; Pink: $1/6<110>$; Yellow: $1/3<001>$; Light Blue: $1/3<111>$. (The snapshots show the distribution of dislocations and twinning at peak stress point as well as at the strain value of 0.2).

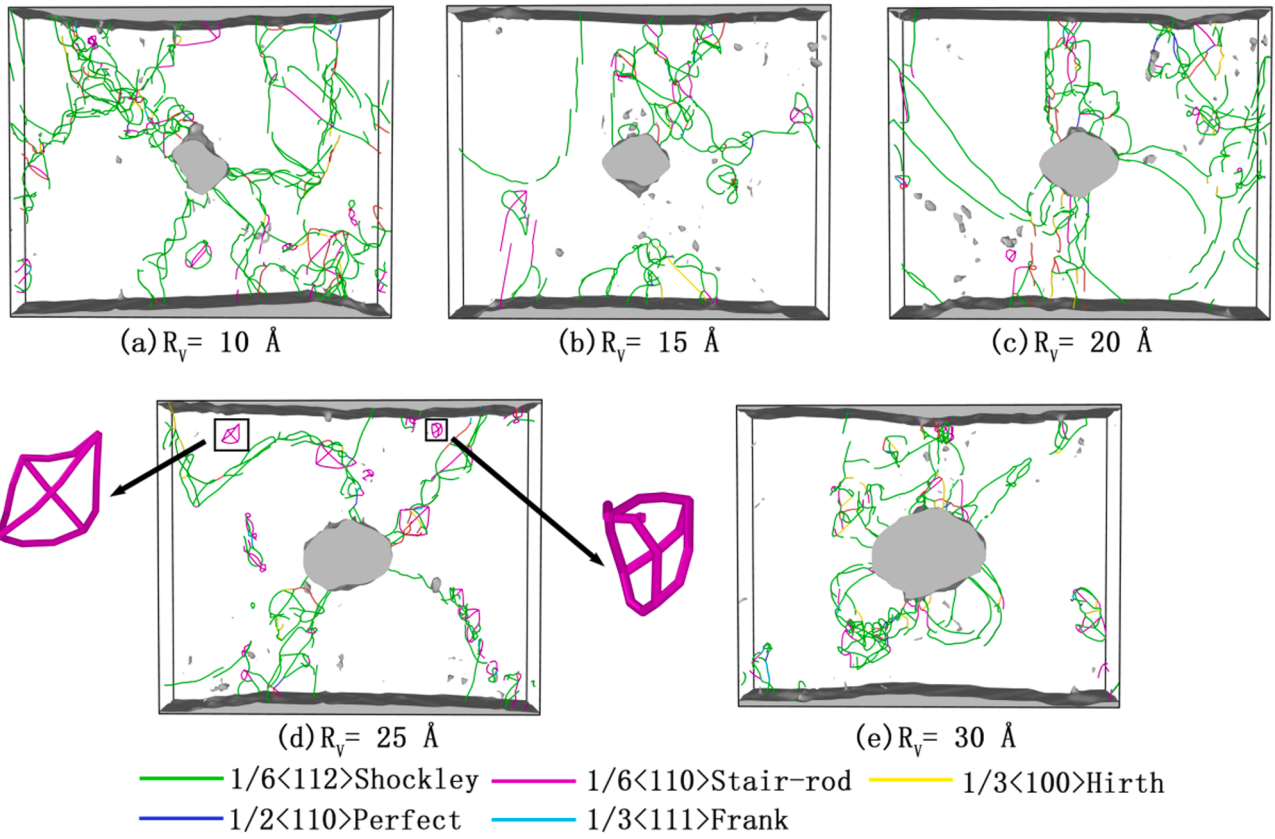


Fig. 15. Distribution of dislocations in FeNiCrCoCu HEA, which has a void with different sizes at a strain rate of $1 \times 10^9 \text{ s}^{-1}$ and 300 K at the strain value of 0.2. Dislocations are colored according to their dislocation styles. Red: other; Green: $1/6<112>$; Blue: $1/2<1 10>$; Pink: $1/6<110>$; Yellow: $1/3<001>$; Light Blue: $1/3<111>$.

model with different void size. The void is the primary cause of dislocation emission, although its size does not significantly affect the dislocation distribution. With the increase of strain, dislocations develop and spread over the entire area. Shockley partial dislocation with a Burgers vector of $1/6<112>$ accounts for a large proportion of the dislocations, followed by stair-rod dislocation with a Burgers vector of $1/6<110>$. In contrast, other dislocations only account for a small fraction. Dislocations originate in the void and propagate to the free surface. However, in the model with the largest void sizes, dislocations are primarily concentrated around the void rather than at the free surface (Fig. 15(e)). During tensile deformation, with an increase in strain, dislocations forms and interact with each other, resulting in the formation of numerous dislocation loops such as stacking fault tetrahedral loops that are possibly formed by dislocation glide and cross slip [84], as shown in Fig. 15(d).

Fig. 16 shows the distribution of dislocations at different temperatures and strain rates from two single-void models with void sizes of 15 Å and 20 Å. Changing the temperature and strain rate leads to significant differences in the dislocation distributions, as expected. The Shockley dislocation is still dominant in all models. As shown in Fig. 16(a–c), the higher temperature increases the number of dislocations and the level of deformation, which results in dislocation concentration at the high deformation area. With increasing temperature, certain unknown dislocations are formed. Similarly, as shown in Fig. 16(d–e), increasing the strain rate generates more dislocations and results in higher deformation of the void, making the dislocations gather in the high deformed region. The amount and distribution of dislocations are clearly influenced by laser-shock-induced ultra-high-strain-rate plastic deformation in FCC-Ni and BCC-Fe [85].

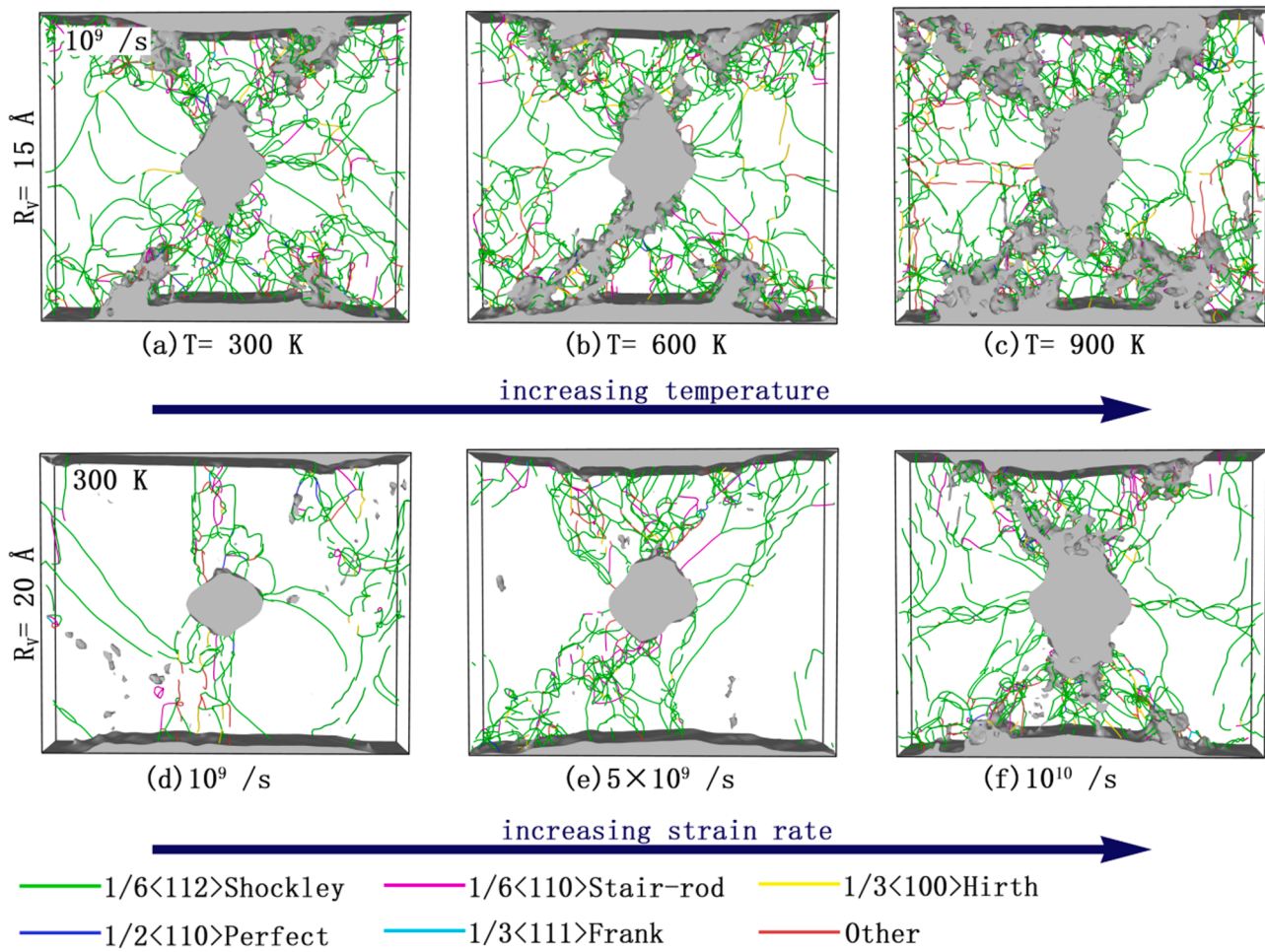


Fig. 16. At the strain value of 0.2, the final distribution of dislocations in single-void FeNiCrCoCu HEA with a void size of 15 Å at temperatures of (a) 300 K, (b) 600 K, or (c) 900 K, or with a void size of 20 Å under the strain rates of (d) $1 \times 10^9 \text{ s}^{-1}$, (e) $5 \times 10^9 \text{ s}^{-1}$, or (f) $1 \times 10^{10} \text{ s}^{-1}$. Dislocations are colored according to their dislocation styles. Red: other; Green: $1/6<112>$; Blue: $1/2<110>$; Pink: $1/6<110>$; Yellow: $1/3<001>$; Light Blue: $1/3<111>$.

4. Future prospects and challenges

Molecular dynamics simulation can simulate the performance evolution rule and failure mechanism of materials under specific conditions, and then improve the material design in experiments, which can provide theoretical guidance for experimental research. Based on MD simulation, the influence of void defects on mechanical properties can be deeply understood from the microstructural level. The viewpoint of defects can provide valuable guidance for the design of HEAs based on defect regulation. With the continuous development of Computational Materials Science, its role will become increasingly important. Recently, with the development of the Materials Genome Initiative, machine learning based on big data has been widely used in alloy design and performance prediction. In the future, machine learning techniques can be used to study the mechanism of the short-range ordered structures on defect deformation behavior of high entropy alloys.

Theoretical calculation can understand the structure and performance of HEAs at the atomic level, which is try to reflect the real scene observed in the experiment. The open database of high entropy materials has not yet formed a standardized format, and the prediction results cannot be calibrated. Due to the multi-element of chemical complexity, theory simulation requires huge computational power. Although large molecular dynamics systems can be processed on high-performance computers, a major bottleneck is the limited choice of general potential functions that can reliably describe metal bonding in HEAs. These limitations hinder the current development of HEAs research.

5. Conclusions

In conclusion, we used molecular dynamics simulations to explore the influences of voids on the mechanical properties of FCC-FeNiCrCoCu HEAs and the microstructural evolution of the HEAs during tensile loading. We found that the existence of voids seriously affects the mechanical parameters of FeNiCrCoCu HEAs. The tensile strength of the single-void model is higher than that of double-void model. The increasing void size decreases the tensile strength and Young's modulus, whether in single-void or double-void models. But void sizes have little effect on flow stress. The tensile strength decreases as temperature increases. The tensile strength slightly increases at strain rates between 10^8 and 10^9 s^{-1} . However, it significantly increases at strain rates of 10^9 to 10^{10} s^{-1} under various strain rates. In local microstructures, the deformation is initially induced around the voids, which causes the presence of stacking faults, twinnings, and disordered structures transformed by FCC structures. In double-void models, dislocation emission occurs between the voids. The dislocations nucleate from the surface of the voids and propagate to the free surface of the models with increasing strain. During the tensile process, the main dislocation types are Shockley partial dislocations and stair-rod dislocations. Stair-rod dislocations reduce the penetration of the shear band. Our research thoroughly explains the void effect on the mechanical properties of FeNiCrCoCu HEAs, which offers a guidance for the material design.

CRediT authorship contribution statement

Tinghong Gao: Conceptualization, Methodology, Data curation, Visualization, Writing – original draft. **Han Song:** Supervision, Investigation, Writing – review & editing. **Bei Wang:** Supervision, Investigation, Writing – review & editing. **Yue Gao:** Supervision, Formal analysis. **Yutao Liu:** Supervision, Investigation, Writing – review & editing. **Quan Xie:** Supervision, Investigation, Writing – review & editing. **Qian Chen:** Supervision, Investigation, Writing – review & editing. **Qingquan Xiao:** Supervision, Investigation, Writing – review & editing. **Yongchao Liang:** Supervision.

Declaration of Competing Interest

The authors declare that they have no known competing financial interests or personal relationships that could have appeared to influence the work reported in this paper.

Data availability

Data will be made available on request.

Acknowledgments

The work was supported by the Industry and Education Combination Innovation Platform of Intelligent Manufacturing and Graduate Joint Training Base at Guizhou University (Grant No: 2020-520000-83-01-324061), the National Natural Science Foundation of China (Grant nos. 51761004, 51661005, 11964005, and 61264004), the Guizhou Province Science and Technology Fund (Grant no. ZK[2021] 051, [2017] 5788, and J[2015] 2050), High level Creative Talent in Guizhou Education Department of China, the Cooperation Project of Science and Technology of Guizhou Province (Grant no. LH[2016] 7430) and High-level Creative Talent Training Program in Guizhou Province of China (Grant No. [2015]4015).

Supplementary materials

Supplementary material associated with this article can be found, in the online version, at doi:[10.1016/j.ijmecsci.2022.107800](https://doi.org/10.1016/j.ijmecsci.2022.107800).

References

- [1] Oliveira JP, Shen J, Zeng Z, Park JM, Choi YT, Schell N, et al. Dissimilar laser welding of a CoCrFeMnNi high entropy alloy to 316 stainless steel. *Scr Mater* 2022; 206:114219.
- [2] Li Z, Zhao S, Ritchie RO, Meyers MA. Mechanical properties of high-entropy alloys with emphasis on face-centered cubic alloys. *Prog Mater Sci* 2019;102:296–345.
- [3] Duan Y, Sun X, Li Z, Ma G, Yu Q, Wei G, et al. High frequency magnetic behavior of FeCoNiMn_xAl_{1-x} high-entropy alloys regulated by ferromagnetic transformation. *J Alloys Compd* 2022;900:163428.
- [4] Wu M, Setiawan RC, Li DY. Benefits of passive element Ti to the resistance of AlCrFeCoNi high-entropy alloy to corrosion and corrosive wear. *Wear* 2022;492:493-204231.
- [5] Wu S, Qiao D, Zhang H, Miao J, Zhao H, Wang J, Lu Y, Wang T, Li T. Microstructure and mechanical properties of C Hf_{0.25}NbTaW_{0.5} refractory high-entropy alloys at room and high temperatures. *J Mater Sci Technol* 2022;97: 229–38.
- [6] Junho Y, Yong Hee J, Woojin A, et al. Effects of deformation-induced martensitic transformation on cryogenic fracture toughness for metastable Si₈V₂Fe_{4.5}Cr_{1.0}Mn₅Co_{3.0} high-entropy alloy. *Acta Mater* 2022;225:117568.
- [7] Edalati P, Mohammadi A, Katabchi M, Edalati K. Microstructure and microhardness of dual-phase high-entropy alloy by high-pressure torsion: twins and stacking faults in FCC and dislocations in BCC. *J Alloys Compd* 2022;894: 162413.
- [8] Yang Y, Zhang S, Huang P, Wang F. Phase transformation-induced strengthening and multistage strain hardening in double-gradient-structured high-entropy alloys. *Appl Phys A* 2022;128(4):258.
- [9] Schneider M, Laplanche G. Effects of temperature on mechanical properties and deformation mechanisms of the equiatomic CrFeNi medium-entropy alloy. *Acta Mater* 2021;204:116470.
- [10] Agrawal P, Shukla S, Gupta S, Agrawal P, Mishra RS. Friction stir gradient alloying: A high-throughput method to explore the influence of V in enabling HCP to BCC transformation in a γ -FCC dominated high entropy alloy. *Appl Mater Today* 2020; 21:100853.
- [11] Jiao W, Li T, Chang X, Lu Y, Yin G, Cao Z, et al. A novel Co-free Al_{0.75}CrFeNi eutectic high entropy alloy with superior mechanical properties. *J Alloys Compd* 2022;902:163814.
- [12] Wang H, Liu P, Chen X, Lu Q, Zhou H. Mechanical properties and corrosion resistance characterization of a novel Co₃₆Fe₃₆Cr₁₈Ni₁₀ high-entropy alloy for bioimplants compared to 316L alloy. *J Alloys Compd* 2022;906:163947.
- [13] Zhang P, Li Z, Liu H, Zhang Y, Li H, Shi C, Liu P, Yan D. Recent progress on the microstructure and properties of high entropy alloy coatings prepared by laser processing technology: a review. *J Manuf Processes* 2022;76:397–411.
- [14] Zhao C, Zhu H, Xie Z. *In-situ* TiC particles strengthen and ductilize Fe_{1.2}MnNi_{0.8}Cr high entropy alloy. *Intermetallics* 2022;140:107398.
- [15] Ji C, Ma A, Jiang J. Mechanical properties and corrosion behavior of novel Al-Mg-Zn-Cu-Si lightweight high entropy alloys. *J Alloys Compd* 2022;900:163508.
- [16] Xing B, Ding Q, Jin B, Zuo X, Zhang N, Yin S. Corrosion resistance and passivation behavior of CoCrFeNi-TiAl high-entropy alloy coatings in acidic solutions. *J Therm Spray Technol* 2022;1-10.
- [17] Zhang LW, Xu JL, Chen J, Huang J, Luo JM. Microstructure and corrosion resistance of AlCoCrFeNi high-entropy alloy coating on sintered NdFeB magnets prepared by HVOF spraying. *J Magn Magn Mater* 2022;551:169136.
- [18] Wu Z, Li B, Chen M, Yang Y, Zheng R, Yuan L, et al. Tailoring magnetic property and corrosion resistance of FeCoNiCuAl high-entropy alloy with Ce additive. *J Alloys Compd* 2022;901:163665.
- [19] Li N, Wu S, Ouyang D, Zhang J, Liu L. Fe-based metallic glass reinforced FeCoCrNiMn high entropy alloy through selective laser melting. *J Alloys Compd* 2020;822:153695.
- [20] Pole M, Sadeghilardjani M, Shittu J, Ayyagari A, Mukherjee S. High temperature wear behavior of refractory high entropy alloys based on 4-5-6 elemental palette. *J Alloys Compd* 2020;843:156004.
- [21] Whitfield TE, Pickering EJ, Owen LR, Senkov ON, Miracle DB, Stone HJ, et al. An assessment of the thermal stability of refractory high entropy superalloys. *J Alloys Compd* 2021;857:157583.
- [22] Lu Q, Chen X, Tian W, Wang H, Liu P, Zhou H, et al. Corrosion behavior of a non-equiatomic CoCrFeNiTi high-entropy alloy: a comparison with 304 stainless steel in simulated body fluids. *J Alloys Compd* 2022;897:163036.
- [23] Wang H, Xie J, Chen Y, Liu W, Zhong W. Effect of CoCrFeNiMn high entropy alloy interlayer on microstructure and mechanical properties of laser-welded NiTi/304 SS joint. *J Mater Res Technol* 2022;18:1028–37.
- [24] Yang K, Fan X, Li B, Li Y, Wang X. Optimisation of superplastic processing parameters for a TiZrHfBeCuNi high entropy bulk metallic glass in the supercooled liquid region. *J Mater Res Technol* 2022;17:1911–21.
- [25] Asghari-Rad P, Nguyen NTC, Zargaran A, Sathyamoorthi P, Kim HS. Deformation-induced grain boundary segregation mediated high-strain rate superplasticity in medium entropy alloy. *Scr Mater* 2022;207:114239.
- [26] Liu L, Zhang Y, Li J, Fan M, Wang X, Wu G, et al. Enhanced strength-ductility synergy via novel bifunctional nano-precipitates in a high-entropy alloy. *Int J Plasticity* 2022;153:103235.
- [27] Kim JK, Kim JH, Park H, Kim JS, Yang G, Kim R, et al. Temperature-dependent universal dislocation structures and transition of plasticity enhancing mechanisms of the Fe₄₀Mn₄₀Co₁₀Cr₁₀ high entropy alloy. *Int J Plasticity* 2022;148:103148.
- [28] Sun ZH, Zhang J, Xin GX, Xie L, Yang LC, Peng Q. Tensile mechanical properties of CoCrFeNiTiAl high entropy alloy via molecular dynamics simulations. *Intermetallics* 2022;142:107444.
- [29] Zhang L, Qian K, Huang J, Liu M, Shibata Y. Molecular dynamics simulation and machine learning of mechanical response in non-equiatomic FeCrNiCoMn high-entropy alloy. *J Mater Res Technol* 2021;13:2043–54.
- [30] Xian X, Lin L, Zhong Z, Zhang C, Chen C, Song K, Cheng J, Wu Y. Precipitation and its strengthening of Cu-rich phase in CrMnFeCoNiCu high-entropy alloys. *Mater Sci Eng A* 2018;713:134–40.
- [31] Ruestes CJ, Farkas D. Dislocation emission and propagation under a nano-indenter in a model high entropy alloy. *Comput Mater Sci* 2022;205:111218.
- [32] Dehkordi ZK, Malekan M, Nili-Ahmabadi M. Superplastic formability of the developed Zr₄₀Hf₁₀Ti₅Al₁₀Cu₂₅Ni₁₀ high entropy bulk metallic glass with enhanced thermal stability. *J Non Cryst Solids* 2022;576:121265.
- [33] Shen Y, Spearot DE. Mobility of dislocations in FeNiCrCoCu high entropy alloys. *Model Simul Mater Sci Eng* 2021;29(8):085017.
- [34] Kretova MA, Konchakov RA, Koblev NP, Khonik VA. Point defects and their properties in the Fe₂₀Ni₂₀Cr₂₀Co₂₀Cu₂₀ high-entropy alloy. *JETP Lett* 2020;111 (12):679–84.
- [35] Liu Y, Li R, Peng Q. The preexisting edge dislocations as recombination center of point defects enhancing irradiation tolerance in CoCrCuFeNi high entropy alloy. *Materialia* 2022;21:101307.
- [36] Peng J, Xie B, Zeng X, Fang Q, Liu B, Liaw PK, et al. Vacancy dependent mechanical behaviors of high-entropy alloy. *Int J Mech Sci* 2022;218:107065.
- [37] Zhao M, Wu T, Liu D, Huang Y, Zhao L, Tang Y, Shen M, Hu Y, Zhang J, Li J, Yu M, Song L. Effect of carbon fiber on microstructure evolution and surface properties of FeCoCrNiCu high-entropy alloy coatings. *Mater Corros* 2019;71(3):430–9.
- [38] Luo G, Li L, Fang Q, Li J, Tian Y, Liu Y, Liu B, Peng J, Liaw PK. Microstructural evolution and mechanical properties of FeCoCrNiCu high entropy alloys: a microstructure-based constitutive model and a molecular dynamics simulation study. *Appl Math Mech* 2021;42(8):1109–22.

- [39] Tian Y, Fang Q, Li J. Molecular dynamics simulations for nanoindentation response of nanotwinned FeNiCrCoCu high entropy alloy. *Nanotechnology* 2020;31(46):465701.
- [40] Zhang L, Shibuta Y. Inverse Hall–Petch relationship of high-entropy alloy by atomistic simulation. *Mater Lett* 2020;274:128024.
- [41] Li J, Dong L, Dong X, Zhao W, Liu J, Xiong J, et al. Study on wear behavior of FeNiCrCoCu high entropy alloy coating on Cu substrate based on molecular dynamics. *Appl Surf Sci* 2021;570:151236.
- [42] Deluigi OR, Pasianot RC, Valencia FJ, Caro A, Farkas D, Bringa EM. Simulations of primary damage in a high entropy alloy: probing enhanced radiation resistance. *Acta Mater* 2021;213:116951.
- [43] Gao Y, Wang B, Huang J, Gao T, Yang W, Xie Q, et al. Growth pattern of homogeneous and heterogeneous nucleation in high-entropy FeNiCrCoCu alloys. *Cryst Growth Des* 2022;24:17–25.
- [44] Xue L, Atli KC, Zhang C, Hite N, Srivastava A, Leff AC, et al. Laser powder bed fusion of defect-free NiTi shape memory alloy parts with superior tensile superelasticity. *Acta Mater* 2022;229:117781.
- [45] Wang FZ, Zhang CH, Cui X, Zhou FQ, Zhang S, Chen HT, Chen J. Effect of energy density on the defects, microstructure, and mechanical properties of selective-laser-melted 24CrNiMo low-alloy steel. *J Mater Eng Perform* 2022;31(5):3520–34.
- [46] Cerri E, Ghio E, Bolelli G. Defect-correlated vickers microhardness of Al-Si-Mg alloy manufactured by laser powder bed fusion with post-process heat treatments. *J Mater Eng Perform* 2022;1:21.
- [47] Robinson J, Stanford M, Arjunan A. Correlation between selective laser melting parameters, pore defects and tensile properties of 99.9 % silver. *Mater Today Commun* 2020;25:101550.
- [48] Robinson J, Arjunan A, Stanford M, Lyall I, Williams C. Effect of silver addition in copper-silver alloys fabricated by laser powder bed fusion *in situ* alloying. *J Alloys Compd* 2021;857:157561.
- [49] Farrisey L, Ludwig M, McHugh PE, et al. An atomistic study of void growth in single crystalline copper. *Comput Mater Sci* 2000;18(1):102–17.
- [50] Marian J, Knap J, Ortiz M. Nanovoid deformation in aluminum under simple shear. *Acta Mater* 2005;53(10):2893–900.
- [51] Needelman A, Tvergaard VF. An analysis of ductile rupture in notched bars. *J Mech Phys Solids* 1984;32(6):461–90.
- [52] Zhao L, Liu Y. Investigation on void growth and coalescence in single crystal copper under high-strain-rate tensile loading by atomistic simulation. *Mech Mater* 2020;151:103615.
- [53] Wang L, Sun J, Li Q, Li Z, Zheng Y. Coupling effect of twin boundary and void on the mechanical properties of bulk nanotwinned copper: an atomistic simulation. *J Phys D Appl Phys* 2019;52(5):055303.
- [54] Liu H, Wang XM, Liang H, Zhao ZN, Li L, Yue ZF, Deng CH. The effect of void defect on the evolution mechanisms of dislocations and mechanical properties in nickel-based superalloys by molecular dynamics simulation of real γ/γ' structures. *Int J Solids Struct* 2020;191–192:464–72.
- [55] Qi Y, Chen X, Feng M. Molecular dynamics-based analysis of the effect of voids and HCP-Phase inclusion on deformation of single-crystal CoCrFeMnNi high-entropy alloy. *Mater Sci Eng A* 2020;791:139444.
- [56] Cui Y, Toku Y, Kimura Y, Ju Y. High-strain-rate void growth in high entropy alloys: suppressed dislocation emission = suppressed void growth. *Scr Mater* 2020;185:12–8.
- [57] Praveen S, Murty BS, Kottada RS. Alloying behavior in multi-component AlCoCrCuFe and NiCoCrCuFe high entropy alloys. *Mater Sci Eng A* 2012;534:83–9.
- [58] Tang T, Kim S, Horstemeyer MF. Molecular dynamics simulations of void growth and coalescence in single crystal magnesium. *Acta Mater* 2010;58(14):4742–59.
- [59] Wen ZX, Wang JP, Wu YW, Zhou KJ, Yue ZF. Atomistic simulation analysis of the effects of void interaction on void growth and coalescence in a metallic system. *Curr Appl Phys* 2018;18(6):744–51.
- [60] Tran AS, Fang TH. Void growth and coalescence in Cu-Ta metallic glasses using molecular dynamics. *Comput Mater Sci* 2019;168:144–53.
- [61] Farkas D, Caro A. Model interatomic potentials and lattice strain in a high-entropy alloy. *J Mater Res* 2018;33(19):3218–25.
- [62] Melchionna S, Ciccotti G, Holian BL. Hoover NPT dynamics for systems varying in shape and size. *Mol Phys* 2006;78(3):533–44.
- [63] Evans DJ, Holian BL. The nose–hoover thermostat. *J Chem Phys* 1985;83(8):4069–74.
- [64] Martys NS, Mountain RD. Velocity Verlet algorithm for dissipative-particle-dynamics-based models of suspensions. *Phys Rev E* 1999;59(3):3733.
- [65] Xie Zhilin, et al. Novel high pressure hexagonal OsB₂ by mechanochemistry. *J Solid State Chem* 2014;215:16–21.
- [66] Hua D, Xia Q, Wang W, Zhou Q, Li S, Qian D, et al. Atomistic insights into the deformation mechanism of a CoCrNi medium entropy alloy under nanoindentation. *Int J Plasticity* 2021;142:102997.
- [67] Plimpton S. Fast parallel algorithms for short-range molecular dynamics. *J Comput Phys* 1995;117(1):1–19.
- [68] Stukowski AJM. Visualization and analysis of atomistic simulation data with OVITO—the open visualization tool. *Simul Mater Sci Eng* 2010;18(1):2154–62.
- [69] Stukowski A, Albe K. Extracting dislocations and non-dislocation crystal defects from atomistic simulation data. *Model Simul Mater Sci Eng* 2010;18(8):085001.
- [70] Stukowski A. Structure identification methods for atomistic simulations of crystalline materials. *Model Simul Mater Sci Eng* 2012;20(4):045021.
- [71] Jung SP, Kwon Y, Lee CS, Lee BJ. Influence of hydrogen on the grain boundary crack propagation in bcc iron: a molecular dynamics simulation. *Comput Mater Sci* 2018;149:424–34.
- [72] Sung PH, Chen TC. Studies of crack growth and propagation of single-crystal nickel by molecular dynamics. *Comput Mater Sci* 2015;102:151–8.
- [73] Chen XX, Ngan AHW. Specimen size and grain size effects on tensile strength of Ag microwires. *Scr Mater* 2011;64(8):717–20.
- [74] Hossain SI, Hasan M, Hasan MN, et al. Effect of chemical treatment on physical, mechanical and thermal properties of ladies finger natural fiber. *Adv Mater Sci Eng* 2013, 2013.
- [75] Choudhuri D, Gwalani B, Gorsse S, Komarasamy M, Mantri SA, Srinivasan SG, Mishra RS, Banerjee R. Enhancing strength and strain hardenability via deformation twinning in fcc-based high entropy alloys reinforced with intermetallic compounds. *Acta Mater* 2019;165:420–30.
- [76] Peng J, Li L, Li F, Liu B, Zherebtsov S, Fang Q, et al. The predicted rate-dependent deformation behaviour and multistage strain hardening in a model heterostructured body-centered cubic high entropy alloy. *Int J Plasticity* 2021;145:103073.
- [77] Dadrasi A, Albooyeh AR, Hamed Mashhadzadeh A. Mechanical properties of silicon-germanium nanotubes: a molecular dynamics study. *Appl Surf Sci* 2019;498:143867.
- [78] Wang L, Liu W, Zhu B, Chen W, Zhang F, Liu B, Liu J, Zhou J, Zhao Y. Influences of strain rate, Al concentration and grain heterogeneity on mechanical behavior of CoNiFeAl_xCu_{1-x} high-entropy alloys: a molecular dynamics simulation. *J Mater Res Technol* 2021;14:2071–84.
- [79] Doan DQ, Fang TH, Chen TH, Bui TX. Effects of void and inclusion sizes on mechanical response and failure mechanism of AlCrCuFeNi₂ high-entropy alloy. *Eng Fracture Mech* 2021;252:107848.
- [80] Vu TN, Pham VT, Nguyen VT, Fang TH. Interfacial strength and deformation mechanism of Ni/Co multilayers under uniaxial tension using molecular dynamics simulation. *Mater Today Commun* 2022;30:103088.
- [81] Lu X, Yang P, Luo J, Ren J, Xue H, Ding Y. Tensile mechanical performance of Ni-Co alloy nanowires by molecular dynamics simulation. *RSC Adv* 2019;9(44):25817–28.
- [82] Kumar R, Panwar V, Gupta MK. Temperature and strain rate dependent tensile behavior of polycrystalline nanocopper under dynamic loading. *Mater Today Proc* 2022;62:44–8.
- [83] Li J, Tian C, Zhang Y, Zhou H, Hu G, Xia R. Structure-property relation of nanoporous graphene membranes. *Carbon* 2020;162:392–401.
- [84] Loretto MH, Phillips PJ, Mills MJ. Stacking fault tetrahedra in metals. *Scr Mater* 2015;94:1–4.
- [85] Zhou W, Ren X, Yang Y, Tong Z, Chen L. Dislocation behavior in nickel and iron during laser shock-induced plastic deformation. *Int J Adv Manuf Technol* 2019;108(4):1073–83.